



Aalborg Universitet

AALBORG UNIVERSITY
DENMARK

Semi-Deterministic Dynamic Millimeter-wave Channel Modeling Based on an Optimal Neural Network Approach

Zhao, Xiongwen; Fu, Zihao; Fan, Wei; Zhang, Yu; Geng, Suiyan; Du, Fei; Qin, Peng; Zhou, Zhenyu; Zhang, Lei

Published in:
I E E E Transactions on Antennas and Propagation

DOI (link to publication from Publisher):
[10.1109/TAP.2022.3145438](https://doi.org/10.1109/TAP.2022.3145438)

Publication date:
2022

Document Version
Accepted author manuscript, peer reviewed version

[Link to publication from Aalborg University](#)

Citation for published version (APA):

Zhao, X., Fu, Z., Fan, W., Zhang, Y., Geng, S., Du, F., Qin, P., Zhou, Z., & Zhang, L. (2022). Semi-Deterministic Dynamic Millimeter-wave Channel Modeling Based on an Optimal Neural Network Approach. *I E E E Transactions on Antennas and Propagation*, 70(6), 4082-4095. <https://doi.org/10.1109/TAP.2022.3145438>

General rights

Copyright and moral rights for the publications made accessible in the public portal are retained by the authors and/or other copyright owners and it is a condition of accessing publications that users recognise and abide by the legal requirements associated with these rights.

- Users may download and print one copy of any publication from the public portal for the purpose of private study or research.
- You may not further distribute the material or use it for any profit-making activity or commercial gain
- You may freely distribute the URL identifying the publication in the public portal -

Take down policy

If you believe that this document breaches copyright please contact us at vbn@aub.aau.dk providing details, and we will remove access to the work immediately and investigate your claim.

Semi-Deterministic Dynamic Millimeter-wave Channel Modeling Based on an Optimal Neural Network Approach

Xiongwen Zhao, *Senior Member, IEEE*, Zihao Fu, Wei Fan, *Senior Member, IEEE*,
 Yu Zhang, Suiyan Geng, Fei Du, Peng Qin, Zhenyu Zhou, *Senior Member, IEEE*, Lei Zhang

Abstract—Billions of mobile terminals will be deployed in various of Internet of Things (IoTs), in which millimeter-wave technology will be gradually applied. Accurate modeling and simulation of wireless channel is the base for efficient design and performance evaluation, this becomes more important for industrial scenarios, which might be highly dynamic and potentially different from well-investigated cellular deployment scenarios. In this work, a novel semi-deterministic millimeter-wave dynamic channel modeling approach based on optimal neural network (ONN) principle is proposed. The ONNs are radial basis function neural networks trained with optimal variance parameters and are applied to predict large-scale channel parameters (e.g., path-loss, delay spread and angle spreads). Based on the ONNs predicted large-scale parameters and the simplified propagation environment including the layout of transmitter, receiver and major scatterers, the proposed channel modeling approach can generate accurate dynamic channel parameters. The proposed approach is validated by the channel data measured at a high-voltage substation. Large-scale parameters, multipath component distribution and power delay profile are validated. The proposed approach is demonstrated to be an accurate, fast and robust channel modeling method, which can be used for both link-level and system-level channel simulation for future design and optimization of industrial IoTs.

Index Terms—Millimeter wave, dynamic channel modeling, optimal neural network, multipath component, map-based channel modeling

I. INTRODUCTION

IN the coming years, billions of mobile terminals and sensors will be deployed in various scenarios, such as smart grid, smart industry and intelligent transportation systems (ITS). Wireless communication, including the fifth generation (5G) and its beyond technologies, will play a major role in Internet of Things (IoT) systems to meet the requirement of high transmission data rate of payload links [1]. Large-scale deployment of 5G commercial systems is ongoing,

This work was supported by the National Nature Science Foundation of China (NSFC) under Grant No. 61931001.

X. Zhao, Z. Fu, Y. Zhang, S. Geng, F. Du, P. Qin and Z. Zhou are with the State Key Laboratory of Alternate Electrical Power System with Renewable Energy Sources, School of Electrical and Electronic Engineering, North China Electric Power University, Beijing 102206, China, and with Hebei Key Laboratory of Power Internet of Things Technology, North China Electric Power University, Baoding, 071003, Hebei, China. (Corresponding author: Zihao Fu, email: fuzihao@ncepu.edu.cn).

W. Fan is with Department of Electronic Systems, Aalborg University, Denmark. (email: wfa@es.aau.dk).

L. Zhang is with the Shandong Electric Power Research Institute, State Grid Corporation of China, Jinan 250002, China (e-mail: 18660130685@163.com).

where the focus has been on sub-6 GHz massive multiple-input multiple-output (MIMO) technology. Millimeter-wave (mmWave) technology is seen essential in 5G hotspot scenarios (which demands high data-rate transmission in dense user scenarios), thanks to its large available system bandwidth [2].

Unlike sub-6 GHz frequency bands, mmWave channel is shown to be highly sparse and specular, making it highly sensitive to environment changes [3] [4]. Furthermore, mmWave suffers from high transmission loss and cannot penetrate objects, which makes it highly dynamic [5]. The dynamic of channel is caused by either the variation of environment or the positions changing of transceiver. Accurate and realistic channel modeling is essential for system design and evaluation. So far, significant efforts have been carried out in the standardization, e.g., in the Third Generation Partnership Project (3GPP) [6], International Telecommunication Union (ITU) [7] and Wireless World Initiative New Radio (WINNER) [8]. However, although various deployment scenarios (e.g., indoor, urban, suburban) are considered, few works have reported channel modeling results in typical power industry hotspot scenarios.

Radio channel modeling is a long-standing and evolving research topic due to its importance. Channel modeling approaches may be grouped into two categories, i.e., deterministic approach and stochastic approach [9]. The deterministic models, e.g., ray tracing (RT) and stored measurement data, are physically meaningful and potentially accurate [10]–[12]. However, RT requires accurate geometric and electromagnetic description of the database, which might not be available. Its computation complexity can also be prohibitive. Furthermore, it is site-specific, which means it is only representative for the scenario considered. As a result, many runs using different environment are required in many cases, leading to more time-consuming simulations. Mobile and wireless communications Enablers for the Twenty-twenty Information Society (METIS) map-based model is a simple ray tracing approach, which aims at reducing computation and modeling complexity yet offers reasonable channel simulation accuracy [13].

Stochastic modeling approach, on the other hand, describes wireless signal propagation using statistical parameters. The most popular and widely accepted stochastic modeling approach is the geometry-based stochastic channel model (GSCM [14]). With the GSCM, the scatterer locations in the environment are selected in a random manner following certain probability distribution, yet the actual channel

impulse response is obtained in a deterministic RT manner. GSCM is widely accepted in the fourth generation (4G) (e.g., 3GPP 25.996 [9]) and 5G standards (e.g., 3GPP 38.901 [6]). However, the GSCM is generally stationary, which might be inaccurate to model highly dynamic mmWave channels. In recent years, dynamic channel modeling and simulation have been widely studied. RT is regarded as an effective approach to investigate dynamic channels [15]. However, its complexity is still a major bottleneck. Semi-dynamic channel modeling based on the GSCM framework is also another popular strategy, where some time evolution features can be added. In [16]–[18], the quasi deterministic radio channel generator (QuaDRiGa) is proposed, which contains dynamic channel modeling capability. In [19], a unified GSCM-based framework is investigated, aiming at capturing non-stationary small-scale fading channel characterization. Besides, GSCM-based dynamic channel models are also investigated for mobile-to-mobile [20] and unmanned aerial vehicle (UAV) [21] scenarios. The main drawback of GSCM-based channel modeling approach is its stochastic nature, which makes it difficult to directly compare with the real-world measurements. Motivated by the main drawbacks of the deterministic and stochastic channel modeling approach, it is highly desirable that the modeling approach should be accurate, realistic yet also computationally efficient.

Due to the excellent performance of nonlinear fitting capability and prediction accuracy offered by machine learning (ML) algorithms, it has been applied extensively in channel modeling research in recent years. The artificial neural network (ANN) based channel modeling approaches have been applied to model path-loss (PL), shadow fading (SF), channel impulse response (CIR), delay spread (DS), angle spread (AS) and multipath components (MPCs). In [22] [23], ANNs are applied to improve the prediction accuracy of outdoor signal received power. Combined with fuzzy logic and ANN, the adaptive neuro-fuzzy inference system is applied to develop PL models in [24]. In [25], a radial basis function (RBF) based PL model is established to investigate the relationship between PL and propagation distance in the mmWave band. In [26], a convolutional neural network (CNN) based model is proposed to predict the PL based on the environment map. A generative adversarial network (GAN) framework is proposed in [27] to achieve autonomous wireless channel modeling.

The ANN-based method is also promising to model dynamic channels. In [28], based on the RT simulated channels, the CNN is applied for channel parameters prediction. In [29], the feed-forward neural network (NN) and RBF NN is applied to predict dynamic receive power, DS and AS, both measured and simulated data are considered. In [30], a ML-based big data application is investigated in channel modeling and parameter prediction, where multiple ANNs are trained by either measurement or simulation data to predict dynamic received power and DS at untrained positions. In [31], the RBF-based channel modeling approaches are proposed to accurately play back time-varying measured channels in terms of MPCs, PL, DS and AS. However, due to limited measured data, only the results of the played back channel in known locations are given in [31], while its ability to predict MPCs

at unknown positions remains to be verified.

As a summary, the dynamic channel modeling approach will be a promising research direction with available big channel data together with geographical database, yet it is not impeccable and some aspects are still not thoroughly addressed in the literature: 1) Traditional RT approaches are characterized by high computational complexity, time-consuming and require accurate environmental information, which makes it difficult to be applied to channel simulations in a complicated environment with irregular scatterers. 2) There has been no reported work on prediction of MPC distribution by the ANN-based approaches due to the complexity associated with mapping between MPC distribution and the propagation environment. To address this topic, it was proposed to combine ANN with other channel models, such as RT in [30]. However, due to the computational complexity of RT, the approach in [30] is not suitable for large-scale simulations. 3) The accuracy of parameters predicted by the ANN-based approaches in case of small data remains to be verified. At present, the measurement data is relatively limited since 5G mmWave massive antenna channel measurements are very time-consuming and expensive. In [28] and [29], the NNs are utilized as an interpolation tool to predict parameters. Besides, the structure of CNN is relative complex in [28], while in [29], fixed parameter settings are applied in the training process of NN, which may cause the inaccurate of prediction results.

In this work, we propose an optimal neural network (ONN) based three-dimensional (3D) semi-deterministic dynamic mmWave channel modeling approach, which considers combining ANN, statistical channel model and environment characteristics. The main purpose of the proposed channel model is to simulate dynamic channels in a complicated environment with irregular scatterers (such as the high-voltage station) where ray tracing is not feasible and only limited measurement data is available. The main contributions and novelties of this paper are summarized as follows:

- A method to optimize neural network by searching the optimal variance parameters of RBF NN is proposed to predict large-scale channel parameters (LSCPs) exactly in case of small training data. The LSCPs include PL, DS, azimuth angular spread of arrive (AASA), elevation angular spread of arrive (EASA) and number of clusters.
- The proposed semi-deterministic dynamic model supports custom simulation scenario as well as trajectory of receiver and scatterers, and it can simulate the paths of main MPCs while maintaining the statistical characteristics of the channel. The LSCPs are predicted by the trained ONNs, and the distribution of MPCs as well as channel coefficients of the dynamic channel are generated according to the geometric relationship and statistical distribution, in which the LSCPs predicted by ONNs are utilized to ensure the spatial continuity of simulated channels.
- The performance of the ONN-based modeling approach is validated by the mmWave channels measured in a high-voltage substation. The measured LSCPs are used to train the ONNs, and the ONN-based simulated channel properties including LSCPs, MPCs distribution and power delay

profile (PDP) are validated by actual measurements and compared with the simulated results from QuaDRiGa.

The remainder of this paper is organized as follows: Section II investigates the proposed ONN-based 3D semi-deterministic dynamic mmWave channel modeling framework. Section III introduces the measured channel data used for model validation. Section IV shows the results and analysis. Conclusions are drawn in Section V.

II. APPROACH DESCRIPTION OF THE ONN-BASED 3D SEMI-DETERMINISTIC DYNAMIC CHANNEL MODEL

In this section, we will elaborate on our proposed channel modeling and simulation process in detail. First of all, a typical single-input multiple-output (SIMO) system wireless communication channel between transmitter (TX) and receiver (RX) is considered, in which one fixed antenna element is deployed at TX and $R \times S$ antenna elements are deployed at RX. The simplified schematic of the channel is shown in Fig. 2. The line-of-sight (LoS) ray is drawn in Fig. 2 with red line. The observable rays are drawn in Fig. 2 with yellow dotted lines, which are reflected or scattered by main scatterers (e.g., ground, buildings and walls). The main scatterers are easy to locate, and they are modeled as determined scatterers, i.e., the coordinates of determined scatterers are set according to the environment. The cluster grouped by these rays is called determined cluster. The non-observable rays are drawn with blue dotted lines in Fig. 2, and they come from multiple reflections or scatterings, whose propagation links with weak power are hardly observed. Besides, those weaker rays present larger delays, which are of low importance since mmWave communications rely on dominant propagation paths. Thus, they are considered coming from randomly generated scatterers, i.e., the coordinates of the scatterers are randomly generated according to the probability distribution. The cluster grouped by these rays is called randomly generated cluster. For clarity, the key parameters involved in the channel modeling and simulation are listed in Table II.

The proposed modeling and simulation procedure is described into five main steps: ONN generation, simulated environment design, LSCPs prediction, small-scale channel parameters (SSCPs) generation and CIR generation. In this

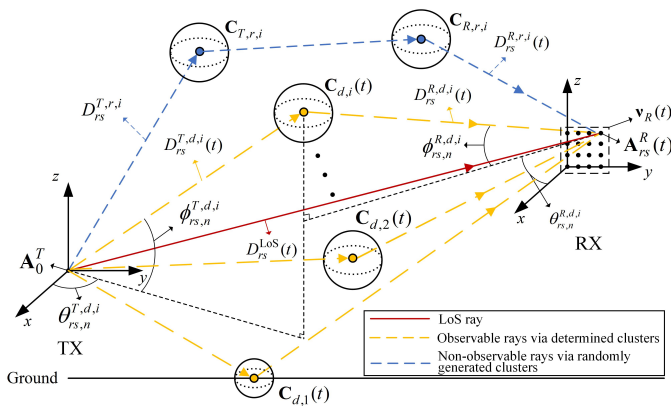


Fig. 1. An abstract scene of SIMO communication scenario.

work, LSCPs include PL, DS, AASA, EASA and number of clusters, and SSCP include power, delay and angles of each ray, and the SSCP are parameters of MPC. Fig. 2 shows the full flow chart of the channel modeling and simulation procedure as well as the relationship between input and output. The details of the procedure are listed as follows:

- First, several ONNs are generated to model the relationship between LSCPs and TX/RX coordinates. Note that one ONN is used to predict only a specific LSCP, and the ONN is trained by the optimal parameter ξ which is found during the training process.
- Second, the simulated environment can be designed according to the simulation requirements, including coordinates of TX and scatterers, as well as the speed and moving trajectory of the RX.
- Third, the 5 LSCPs are predicted by the ONNs according to the TX/RX coordinates at time instant t .
- Fourth, the SSCP of LoS ray are directly derived by the geometric relationship according to the TX/RX coordinates. The SSCP of remaining rays are generated in two steps: 1) generation of cluster parameters: the cluster parameters of determined cluster are derived by the geometric relationship according to the TX/RX coordinates, while those of randomly generated cluster are generated by statistical distribution according to the predicted AASA/EASA; 2) generation of SSCP: the SSCP of rays in determined and randomly generated clusters are calculated by the statistical distribution according to the predicted DS and cluster parameters.
- Finally, the dynamic CIRs can be directly generated by the simulated SSCP. The principle of each sub-step will be described in more details in the following subsections.

A. Optimal Neural Network Generation

The generation process of ONN is discussed in detail in this sub-section. We first introduce the structure of RBF NN, then the influence of parameter ξ on prediction error is discussed, and the state-of-art methods to determine ξ value in existing works are revisited and analyzed. Finally, the generation process of ONNs based on the Simulated Annealing (SA) algorithm is elaborated.

1) *The structure of RBF NN*: In this work, RBF NN is considered to train the relationship between TX/RX coordinates and LSCPs due to its advantage of nonlinear relationship approximation capability and simple structure. The simplified diagram of input and output mapping in RBF NN is shown in Fig. 3, the structure of RBF NN contains 6 input nodes, 1 output node, several hidden nodes and 1 tunable parameter. The 6 input nodes are the three-dimensional coordinates of the RX and TX position, and one corresponding LSCP value can be predicted by the output node. Note that in this work, each RBF NN is trained to export only one LSCP parameter, in order to reduce the difficulty of training. The input nodes and the hidden nodes are connected by nonlinear transformation layer, while the output node and the hidden nodes are connected by linear combination layer. The variance of RBF ξ is a tunable parameter which acts on the nonlinear transformation layer.

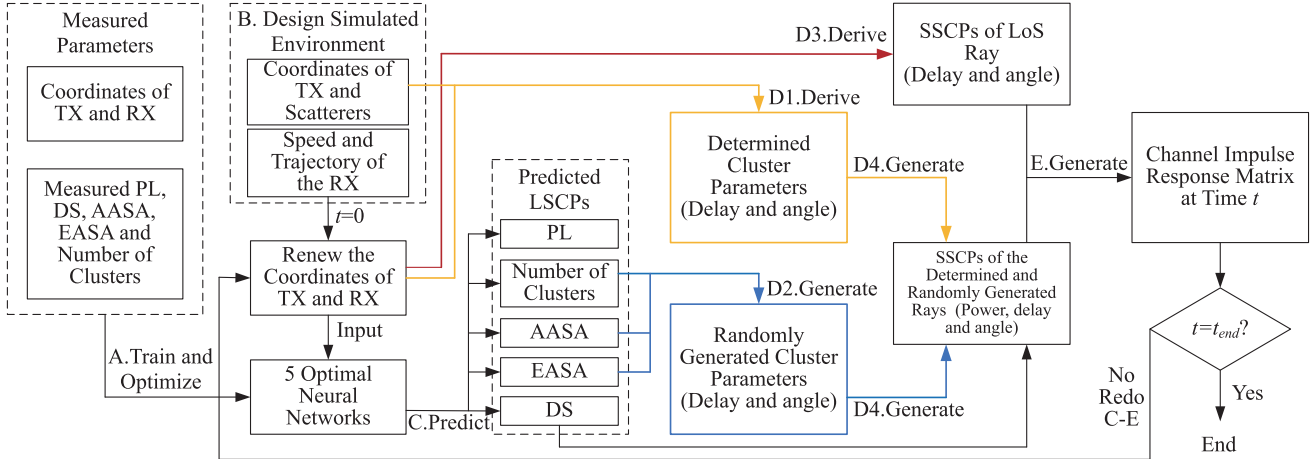


Fig. 2. The modeling and simulation flow chart of the proposed model.

TABLE I
DEFINITION OF SIGNIFICANT CHANNEL MODELING PARAMETERS

Symbol	Definition
\mathbf{A}_0^T	Coordinates of TX antenna element
$\mathbf{A}_{00}^R(t) / \mathbf{A}_{rs}^R(t)$	Coordinates of the first/the r -th row and s -th column RX antenna element
$\mathbf{C}_{d,i}(t)$	Coordinate of the center of the i -th determined scatterer
$\mathbf{C}_{T,r,i}/\mathbf{C}_{R,r,i}$	Coordinate of the center of the i -th randomly generated scatterers
λ_H/λ_V	Horizontal/vertical antenna spacing of the UPA in RX
$\mathbf{v}_R(t)$	The velocity vector of RX at time t
$\theta_{rs}^{T,\text{LoS}}/\phi_{rs}^{T,\text{LoS}}/\theta_{rs}^{R,\text{LoS}}/\phi_{rs}^{R,\text{LoS}}$	AAoD/EAoD/AAoA/EAoA of the LoS ray
$\theta_{rs,n}^{T,d,i}/\phi_{rs,n}^{T,d,i}/\theta_{rs,n}^{R,d,i}/\phi_{rs,n}^{R,d,i}$	AAoD/EAoD/AAoA/EAoA of the n -th ray in the i -th determined cluster
$\theta_{rs,n}^{T,r,i}/\theta_{rs,n}^{T,r,i}/\theta_{rs,n}^{R,r,i}/\phi_{rs,n}^{R,r,i}$	AAoD/EAoD/AAoA/EAoA of the n -th ray in the i -th randomly generated cluster
$D_{rs}^{\text{LoS}}(t)$	Distance between TX and RX
$D_{rs}^{T,d,i}(t)/D_{rs}^{R,d,i}(t)$	Distance between TX/RX and $\mathbf{C}_{d,i}$
$D_{rs}^{T,r,i}(t)/D_{rs}^{R,r,i}(t)$	Distance between TX/RX and $\mathbf{C}_{T,r,i}/\mathbf{C}_{R,r,i}$
$CN(t)$	The total number of clusters at time t
L_n	The total number of rays in each cluster

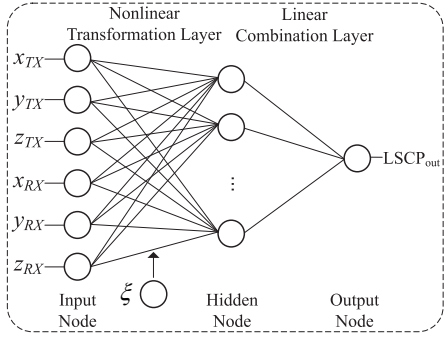


Fig. 3. Simplified diagram of input and output mapping in RBF NN.

The mentioned nodes, layers and parameter together constitute the structure of RBF NN and the k -th predicted LSCP $Y_{k,\text{out}}$ can be simply expressed as

$$Y_{k,\text{out}} = M(x_{R,k}, y_{R,k}, z_{R,k}, x_{T,k}, y_{T,k}, z_{T,k}, \xi), \quad (1)$$

where M denotes the mapping of the input and output. The prediction performance is validated by the root mean square error (RMSE) between the predicted and measured values

$$E_{\text{RMSE}} = \sqrt{\frac{1}{K} \sum_{k=1}^K (Y_{k,\text{out}} - Y_{k,\text{act}})^2}, \quad (2)$$

where K is the total number of predicted values and $Y_{k,\text{act}}$ is the k -th actual value. Note that both $Y_{k,\text{out}}$ and $Y_{k,\text{act}}$ are represented for their real values and are not normalized, and we use different RMSE values to evaluate the prediction performance of different LSCPs.

2) *The influence of parameter ξ on prediction error:* The prediction error of NN is affected by several factors, such as the amount of data, dataset selection and parameters settings. In this work, the prediction error can be reduced by determining the optimal value ξ . Generally speaking, the value of ξ should be set large enough to ensure that the response range of input node should cover different input vectors. However, if the value of ξ is set too large, different

input nodes may have an overlapping response area, which would reduce the prediction accuracy.

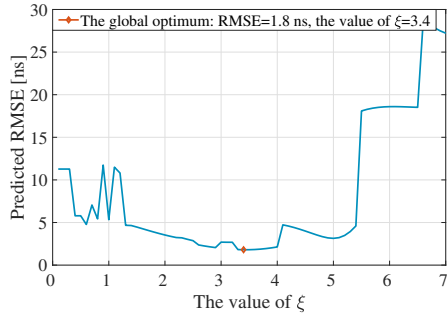


Fig. 4. Predicted RMSEs of the RBF NN trained with different ξ values.

Fig. 4 shows the predicted RMSE curve for the RBF NN trained with different ξ values. Note that the RBF NN here is used to predict the DS, and a similar trend is existed when using the RBF NNs in predicting other types of LSCPs. It is seen in Fig. 4 that the prediction RMSE decreases first and then increases with the increase of ξ value, as expected. Thus, the main challenge of generating ONN is to search the optimal ξ value in an efficient way. The expression of the optimal ξ value can be derived according to the structure of RBF NN and (2), and the detailed derivation for (3) is given in Appendix A

$$\begin{aligned} \xi^* &= \arg \min_{\xi} E_{\text{RMSE}} \\ &= \arg \min_{\xi} \sqrt{\frac{1}{K} \sum_{k=1}^K \left(\sum_{i=1}^W \left[w_{ik} \cdot e^{-\frac{(\mathbf{q}-\mathbf{w}_i)^T(\mathbf{q}-\mathbf{w}_i)}{2\xi^2}} + b_{ik} \right] - Y_{k,act} \right)^2} \end{aligned} \quad (3)$$

where W is the number of hidden nodes which is determined by the total number of input vectors, w_{ik} and b_{ik} are the connection weight and offset of the linear combination layer, respectively, and they are updated by the back propagation algorithm during the training process. $\mathbf{q} = [x_T, y_T, z_T, x_R, y_R, z_R]$ is the 6-dimensional input vector and w_i is the weight matrix of the nonlinear transformation layer. Note that the variable w_{ik} and b_{ik} will constantly change during the training process, which means the optimal value of ξ cannot be directly derived by (3).

The determination of ξ value has been discussed in some existing works. In [29], the value of ξ is fixed during the training of RBF NN. An estimation method for determining the value of ξ is given in [32]. However, these methods have certain subjective factors, leading to non-optimal ξ value. In order to obtain the NN with lowest prediction error, global search algorithms are considered in the training of RBF NN. The most commonly used algorithms are annealing (SA) [33] and particle swarm optimization (PSO) [34] algorithm. The SA algorithm is a random optimization algorithm based on the Monte-Carlo strategy, it enables the search to jump out of the local optimum via randomly updating new solutions and accepting worse solutions with certain probability, thus in this work, the SA algorithm is adapted as the approach to searching the optima value of ξ .

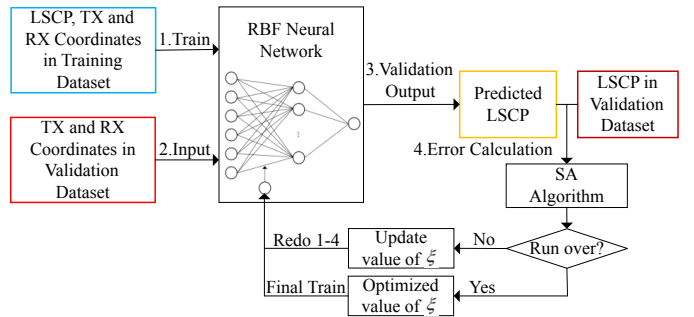


Fig. 5. The ONN generation process based on the adjusted SA algorithm.

3) The ONN generation process based on the SA algorithm:

Fig. 5 shows the generation process of ONN by applying the SA algorithm. Each dataset includes 7 data, i.e., 6 coordinates values and 1 corresponding LSCP value, and the total number of datasets is K . The K datasets are divided into two parts according to a certain proportion, namely training datasets and validation datasets. The training datasets are used to train the RBF NN, then we input the validation TX and RX coordinates information and obtain predicted LSCPs. The RMSE between predicted and actual LSCPs is calculated, and the value of ξ is updated according to the SA algorithm [33], then we continue training the RBF NN until the optimal value of ξ is determined. Finally, the ONNs can be trained with the optimal value of ξ .

B. Simulated environment design

In this sub-section, the environment parameters required by dynamic simulation is introduced. As the Fig. 1 shows, the initial coordinates of TX can be set as $\mathbf{A}_0^T = [0 \ 0 \ H_T]$, and H_T is the antenna height of TX. According to the preset environment, the coordinates of the i -th determined scatterer can be estimated as $\mathbf{C}_{d,i}(t) = [x_{d,i} \ y_{d,i} \ z_{d,i}]$, and the number of determined scatterers are customized by actual deployment scenario. The initial coordinates of RX can be customized as $\mathbf{A}_{00}^R(0)$, and the coordinates of the r -th row and s -th column antenna element can be expressed as

$$\mathbf{A}_{rs}^R(0) = \mathbf{A}_{00}^R(0) + (r-1) \cdot \lambda_H \cdot [0 \ 1 \ 0] + (s-1) \cdot \lambda_V \cdot [0 \ 0 \ 1]. \quad (4)$$

Then according to the customized RX trajectory, the coordinate of RX at time instant t can be derived as

$$\mathbf{A}_{rs}^R(t) = \mathbf{A}_{rs}^R(0) + \int_0^t \mathbf{v}_R(t), \mathbf{v}_R(t) = [v_x(t), v_y(t), v_z(t)], \quad (5)$$

where $v_x(t), v_y(t), v_z(t)$ are the RX velocity components decomposed on the x, y and z axes, respectively.

C. LSCPs prediction

Based on the generation process in sub-section A, five ONNs are trained to predict the 5 parameters, i.e., PL, DS, AASA, EASA and number of clusters, respectively. By utilizing the 3D coordinates of TX and RX at time instant t , the LSCPs can be predicted. Taking DS as an example

$$DS(t) = M_{DS}(x_{R,t}, y_{R,t}, z_{R,t}, x_{T,t}, y_{T,t}, z_{T,t}), \quad (6)$$

where M_{DS} is the trained relationship between coordinates and DS. Similar to (6), the remaining LSCPs can also be predicted. Note that total number of clusters can be decomposed as the sum of number of determined and randomly generated clusters $CN(t) = CN_d(t) + CN_r(t)$, where $CN_d(t)$ and $CN_r(t)$ are the number of determined and randomly generated clusters, respectively.

D. SSCPs Generation

The generation of SSCPs can be decomposed into 4 sub-steps, the sub-step a and b respectively generate the cluster parameters for determined cluster and randomly generated cluster. The sub-step c and d respectively generate the SSCPs for LoS ray and the remaining rays.

1) Determined cluster parameter derivation: After setting the coordinates of TX, RX and clusters at time instant t , the parameters of determined clusters can be directly derived according to geometry relationships. The cluster vectors of the i -th determined cluster can be expressed as

$$\mathbf{r}_{rs}^{R,d,i}(t) = \mathbf{A}_{rs}^R(t) - \mathbf{C}_{d,i}(t) = [x_{rs}^{R,d,i} \ y_{rs}^{R,d,i} \ z_{rs}^{R,d,i}], \quad (7)$$

$$\mathbf{r}_{rs}^{T,d,i}(t) = \mathbf{C}_{d,i}(t) - \mathbf{A}_0^T = [x_{rs}^{T,d,i} \ y_{rs}^{T,d,i} \ z_{rs}^{T,d,i}]. \quad (8)$$

Based on the cluster vector, the cluster delay of the i -th determined cluster is expressed as $\tau_{rs}^{d,i}(t) = (D_{rs}^{R,d,i}(t) + D_{rs}^{T,d,i}(t)) / c$, where $D_{rs}^{T,d,i}(t) = \|\mathbf{r}_{rs}^{T,d,i}(t)\|$ and $D_{rs}^{R,d,i}(t) = \|\mathbf{r}_{rs}^{R,d,i}(t)\|$ are the distance between the center of the i -th determined cluster to TX antenna and the r -th row, s -th column RX antenna element, respectively. Then the azimuth angle of arrival (AAoA) and elevation angle of arrival (EAoA) of the i -th determined cluster can be expressed as

$$\theta_{rs}^{R,d,i} = \arctan_2(y_{rs}^{R,d,i}, x_{rs}^{R,d,i}), \quad (9)$$

$$\phi_{rs}^{R,d,i} = \arcsin(z_{rs}^{R,d,i}, D_{rs}^{R,d,i}), \quad (10)$$

where $\arctan_2(\cdot)$ is the four-quadrant inverse tangent operation. Similar to (9) and (10), the azimuth angle of departure (AAoD) and elevation angle of departure (EAoD) of the i -th determined cluster can also be derived.

2) Randomly generated cluster parameter calculation: For each new randomly generated cluster (the total number of randomly generated clusters is $CN_r(t)$ at time instant t), the 3D coordinates are generated according to the AASA and EASA predicted by the ONNs. The specific position of a randomly generated cluster is calculated by AAoA, AAoD, EAoA, EAoD and distance. For time instant t , the azimuth and elevation angle can be generated as [21]

$$\theta_{rs}^{R,r,i} = Z_A^R \cdot AASA(t) + \partial_A^R, \quad (11)$$

$$\phi_{rs}^{R,r,i} = Z_E^R \cdot EASA(t) + \partial_E^R, \quad (12)$$

where Z_A^R and Z_E^R follow normal distribution $\mathcal{N}(0,1)$, $AASA(t)$ and $EASA(t)$ are the predicted AASA and EASA at time instant t , respectively. ∂_A^R and ∂_E^R are mean values of AAoA and EAoA, respectively. Similar to (11) and (12), $\theta_{rs}^{T,r,i}$ and $\phi_{rs}^{T,r,i}$ can also be calculated. Then the coordinates of

center of the i -th randomly generated scatterers $C_{T,r,i}/C_{R,r,i}$ are derived respectively by

$$\mathbf{C}_{T,r,i} = \mathbf{A}_0^T + D_{rs}^{T,r,i} \cdot \begin{bmatrix} \cos \theta_{rs}^{T,r,i} \cdot \cos \phi_{rs}^{T,r,i} \\ \sin \theta_{rs}^{T,r,i} \cdot \cos \phi_{rs}^{T,r,i} \\ \sin \phi_{rs}^{T,r,i} \end{bmatrix}, \quad (13)$$

$$\mathbf{C}_{R,r,i} = \mathbf{A}_{rs}^R(t) + D_{rs}^{R,r,i} \cdot \begin{bmatrix} \cos \theta_{rs}^{R,r,i} \cdot \cos \phi_{rs}^{R,r,i} \\ \sin \theta_{rs}^{R,r,i} \cdot \cos \phi_{rs}^{R,r,i} \\ \sin \phi_{rs}^{R,r,i} \end{bmatrix}, \quad (14)$$

where $D_{rs}^{R,r,i}$ and $D_{rs}^{T,r,i}$ are the distances between the i -th randomly generated scatterers and RX/TX, respectively, which are defined as a non-negative variable in accordance with exponential distribution [35]. Finally, the cluster delay of the i -th randomly generated cluster is calculated as

$$\tau_{rs}^{r,i}(t) = (D_{rs}^{R,r,i} + D_{rs}^{T,r,i} + \|\mathbf{C}_{T,r,i} - \mathbf{C}_{R,r,i}\|) / c. \quad (15)$$

3) SSCPs determination of the LoS ray: In the proposed channel model, each ray has 6 SSCPs, which are power, delay, AAoA, EAoA, AAoA and EAoD. The SSCPs of LoS ray can be directly derived by the geometrical relationship. Similar to the calculation of cluster vectors, the LoS vector can be expressed as

$$\mathbf{r}_{rs}^{\text{LoS}}(t) = \mathbf{A}_{rs}^R(t) - \mathbf{A}_0^T = [x_{rs}^{\text{LoS}} \ y_{rs}^{\text{LoS}} \ z_{rs}^{\text{LoS}}]. \quad (16)$$

Based on the LoS vector, AAoA and EAoA of the LoS cluster can be calculated as

$$\theta_{rs}^{\text{R,LoS}} = \arctan_2(y_{rs}^{\text{LoS}}, x_{rs}^{\text{LoS}}), \quad (17)$$

$$\phi_{rs}^{\text{R,LoS}} = \arcsin(z_{rs}^{\text{LoS}}, D_{rs}^{\text{LoS}}(t)), \quad (18)$$

where $D_{rs}^{\text{LoS}}(t) = \|\mathbf{r}_{rs}^{\text{LoS}}(t)\|$ is the distance between the TX antenna element from the r -th row, s -th column RX antenna element. Meanwhile, according to geometric symmetry relations, the AAoD and EAoD of the LoS ray can be derived as $\theta_{rs}^{\text{T,LoS}} = \pi - \theta_{rs}^{\text{R,LoS}}$ and $\phi_{rs}^{\text{T,LoS}} = -\phi_{rs}^{\text{R,LoS}}$, respectively. Besides, the delay of LoS ray is calculated by $\tau_{rs}^{\text{LoS}}(t) = D_{rs}^{\text{LoS}}(t)/c$.

4) SSCPs generation of the determined and randomly generated rays: In this work, the generation method of the SSCPs of determined and randomly generated rays are the same. For each ray, the SSCPs are generated by both cluster parameters and predicted DS. The delay of the n -th ray in the i -th determined or randomly generated cluster can be expressed by [6]

$$\tau_{rs,n}^{\Theta,i}(t) = \tau_{rs}^{\Theta,i}(t) - m_\tau \cdot DS(t) \cdot \ln(X_\tau), \quad (19)$$

where X_τ is uniformly distributed within $(0,1)$, m_τ is the delay scalar and $\Theta = \{d, r\}$. The AAoA and EAoA of the n -th ray in one cluster can be calculated by adding the angular offset

$$[\theta_{rs,n}^{\Theta,i}(t), \phi_{rs,n}^{\Theta,i}(t)]^T = [\theta_{rs}^{\Theta,i}(t), \phi_{rs}^{\Theta,i}(t)]^T + [\Delta\theta^R, \Delta\phi^R]^T, \quad (20)$$

where $\Delta\theta^R$ and $\Delta\phi^R$ are angular offsets which are assumed to follow Laplace distributions [19] with zero mean and standard deviation of 1 degree. Note that the standard deviation should be modified subjected to actual measured values to match the

environment. Similar to (20), the AAoD and EAoD of the n -th ray can be also calculated. Finally, based on the time-variant ray delays, the power of the n -th ray in the i -th determined or randomly generated cluster can be generated according to an exponential distribution [6] [21]

$$P_{rs,n}^{\Theta,i}(t) = \exp\left(-\tau_{rs,n}^{\Theta,i}(t)\frac{m_\tau - 1}{m_\tau \cdot DS(t)}\right). \quad (21)$$

E. CIR generation

In the end, the CIR matrix $h_{rs}(t, \tau)$ can be generated by the SSCPs of all the rays, and it is used to describe the small-scale fading of dynamic channel. The complex CIR matrix of wireless channel between the TX antenna element and the r -th row, s -th column RX antenna element can be calculated by the superposition of the LoS, observable and non-observable components, i.e.,

$$h_{rs}(t, \tau) = \sqrt{\frac{1}{K_R + 1}} (K_R \cdot h_{rs}^{\text{LoS}}(t, \tau) + h_{rs}^{\text{obs}}(t, \tau) + h_{rs}^{\text{nobs}}(t, \tau)) \quad (22)$$

where K_R is the K-factor. The LoS component $h_{rs}^{\text{LoS}}(t, \tau)$ can be generated as

$$\begin{aligned} h_{rs}^{\text{LoS}}(t, \tau) &= \begin{bmatrix} F_{rs,V}(\theta_{rs}^{R,\text{LoS}}, \phi_{rs}^{R,\text{LoS}}) \\ F_{rs,H}(\theta_{rs}^{R,\text{LoS}}, \phi_{rs}^{R,\text{LoS}}) \end{bmatrix}^T \begin{bmatrix} e^{j\Phi_{\text{LoS}}^{VV}} & 0 \\ 0 & e^{j\Phi_{\text{LoS}}^{HH}} \end{bmatrix} \\ &\left[\begin{bmatrix} F_{0,V}(\theta_{rs}^{T,\text{LoS}}, \phi_{rs}^{T,\text{LoS}}) \\ F_{0,H}(\theta_{rs}^{T,\text{LoS}}, \phi_{rs}^{T,\text{LoS}}) \end{bmatrix} \cdot e^{j2\pi f_c \tau_{rs}^{\text{LoS}}(t)} \cdot \delta(\tau - \tau_{rs}^{\text{LoS}}(t)) \cdot e^{j2\pi\nu(t)t} \right], \end{aligned} \quad (23)$$

where $j = \sqrt{-1}$, f_c is the carrier frequency, $\{\cdot\}^T$ denotes transposition, $F_{rs/0,V}$ and $F_{rs/0,H}$ are the antenna patterns of RX/TX for vertical and horizontal polarizations, respectively. Besides, Φ_{LoS}^{VV} and Φ_{LoS}^{HH} are random phases subject to uniform distribution in $(0, 2\pi]$, and $\nu(t)$ is the doppler frequency shift, which can be calculated as

$$\nu(t) = \frac{\mathbf{v}_R(t)}{\lambda_c} \cdot \cos \theta_{\mathbf{v}\mathbf{r}}, \quad (24)$$

where λ_c is the wavelength and $\lambda_c = c/f_c$, $\theta_{\mathbf{v}\mathbf{r}}$ is the included angle between the LoS vector $\mathbf{r}_{rs}^{\text{LoS}}(t)$ and the velocity vector $\mathbf{v}_R(t)$. The observable component $h_{rs}^{\text{obs}}(t, \tau)$ can be generated by the SSCPs of the determined rays

$$\begin{aligned} h_{rs}^{\text{obs}}(t, \tau) &= \sum_{i=1}^{CN_d(t)} \sum_{n=1}^{L_n} \begin{bmatrix} F_{rs,V}(\theta_{rs,n}^{R,d,i}, \varphi_{rs,n}^{R,d,i}) \\ F_{rs,H}(\theta_{rs,n}^{R,d,i}, \varphi_{rs,n}^{R,d,i}) \end{bmatrix}^T \\ &\left[\begin{bmatrix} e^{j\Phi_{d,i}^{VV}} & \sqrt{\kappa_{d,i}^{-1}} e^{j\Phi_{d,i}^{VH}} \\ \sqrt{\kappa_{d,i}^{-1}} e^{j\Phi_{d,i}^{HV}} & e^{j\Phi_{d,i}^{HH}} \end{bmatrix} \begin{bmatrix} F_{0,V}(\theta_{rs,n}^{T,d,i}, \varphi_{rs,n}^{T,d,i}) \\ F_{0,H}(\theta_{rs,n}^{T,d,i}, \varphi_{rs,n}^{T,d,i}) \end{bmatrix} \right] \\ &\sqrt{P_{rs,n}^{d,i}(t)} \cdot e^{2\pi j f_c \tau_{rs,n}^{d,i}(t)} \cdot \delta(\tau - \tau_{rs,n}^{d,i}(t)) \cdot e^{j2\pi\nu(t)t}, \end{aligned} \quad (25)$$

where Φ_d^{VV} , Φ_d^{VH} , Φ_d^{HV} , Φ_d^{HH} are the initial phases subject to uniform distribution in $(0, 2\pi]$, κ is the cross-polarization power ratio and L_n is the number of rays in each cluster. Similar to (25), the non-observable component $h_{rs}^{\text{nobs}}(t, \tau)$ can be also generated by the SSCPs of the randomly generated rays.

Note that (22)-(25) can support dynamic channel simulation in a non-line-of-sight (NLoS) case as well by removing the LoS ray component in generation of the CIR.

F. Supplementary Description

In order to maintain the dynamic characteristics and parameter continuities of the proposed model, the birth and death rules of clusters are specified as follows: 1) in general, LoS component and determined clusters are always present, and only the number of randomly generated clusters is updated; 2) if $CN(t+1) > CN(t)$ is met, i.e., the number of clusters at the time instant $t+1$ is greater than that at time instant t , new randomly generated cluster(s) will be added, and the other clusters will not change; 3) if $CN(t+1) < CN(t)$ is met, i.e., the number of clusters at the time instant $t+1$ is less than that at time instant t , the randomly generated clusters with the largest delay will die, and the other clusters will not change.

Note that the proposed 3D semi-deterministic channel model can support both standard geometry based stochastic channel modeling as well as deterministic channel modeling: 1) if the determined scatterers are not set, the channel model can be simplified to traditional statistical model and can simulate mmWave channels which only conforms to the statistical distribution; 2) if the randomly generated scatterers are not set, i.e., all the coordinates of scatterers are determined, the channel model can be approximated as ray tracing, where however the difficulty of setting up the simulation environment and the computations of the parameter calculations will also increase due to the added massive scatterers.

III. MEASUREMENT DATA FOR MODEL VALIDATION

In this work, the proposed ONN-based semi-deterministic dynamic channel modeling approach is validated by the 28 GHz mmWave channel measured data. In this section, the measurement campaigns are first introduced, and the parameters calculation approach is discussed in detail.

A. Measurement Campaigns

The 28 GHz mmWave channel measurement campaign was conducted at a 220 kV high-voltage substation located in Qingdao, China using Keysight time-domain channel sounder [36]. At the high-voltage substation, the environment is relatively static, and the scatterers between the TX and RX include power equipment, such as voltage and current transformers, various types of wires, as well as trees and walls, etc. Figs. 6 (a) and (b) show the measurement environment for the TX and RX equipment of the channel sounder, respectively. It can be seen from Fig. 6 that the environment is complicated, there are many towers, wires and railings in the substation, which makes it impossible to model the environment and use the RT.

The layout of transceiver locations of the channel measurement is shown in Fig. 7, in which the TX was located at the fixed position marked with a rectangle, and the RX was located at a total of 27 positions marked with black circles along the LoS route. The distance between two adjacent measurement positions is 5 m, except for positions 7 and 8, with a distance of 20 m. The length of the measurement route is 150 m. The actual environment in Fig. 7 can be simplified to the abstract scene in Fig. 1. In Fig. 7, the LoS ray always exists and its path is marked with a red line. There are some observable rays

reflected or refracted by the ground or power facilities whose paths are marked with yellow dashed lines. The approximate paths of non-observable rays are marked with blue lines.

An omni-directional antenna with 3 dBi gain is applied at the TX with the height of 2.5 m, while a uniform linear array (ULA) with 8 array elements (ULA-8) is applied at the RX with the height of 2.0 m, and the ULA-8 are connected with eight individual radio frequency (RF) channels at the receiver side of the Keysight channel sounder. By moving the ULA-8 antenna eight times horizontally and eight times vertically, an 8×64 virtual uniform planner array (VUPA) can be generated, which results in a virtual SIMO system. Similar strategy was reported in [37] to improve the spatial resolution of the channel sounding system. The spacing between two adjacent antenna elements of the VUPA is half-wavelength of electromagnetic wave at 28 GHz (i.e., 5.36 mm). The SIMO system will be used for extracting multipath information from measured CIRs later. Back-to-back system calibration was performed before the measurement to eliminate the inherent system response [36]. Specific measurement parameters are can be found in previous work [38].

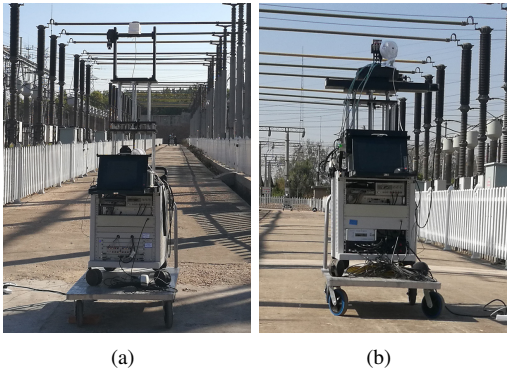


Fig. 6. Measurement environments of the Qingdao high-voltage substation. (a) Transmitter. (b) Receiver.

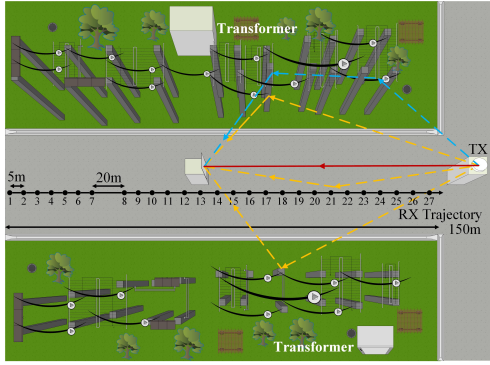


Fig. 7. Simplified schematic diagram of the measurement layout.

B. Parameters Calculation Approach

In this work, the channel parameters required in the modeling and simulation are extracted from the raw channel data, and the full flow chart of channel measurement and data post-processing are shown in Fig. 8. The raw measured data is

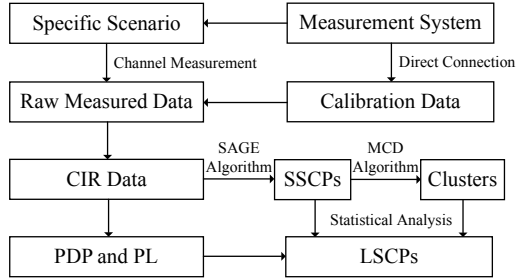


Fig. 8. Flow chart of the data post-processing.

TABLE II
CHANNEL PARAMETERS OF THE HIGH-VOLTAGE SUBSTAION

Parameter	Value	Parameter	Value		
PL	PL_0	61.38	EASA [$\lg(\cdot)$]	μ_{EASA}	1.32
[dB]	n	2.46	σ_{EASA}	0.12	
	σ_{X_s}	4.12	Number of Clusters	μ_C	7.15
DS	μ_{DS}	-8.29	σ_C	1.94	
[$\lg(s)$]	σ_{DS}	0.24	Cluster DS [ns]	-	2.82
AASA	μ_{AASA}	1.5	Cluster AASA [$^\circ$]	-	7.37
[$\lg(\cdot)$]	σ_{AASA}	0.045	Cluster EASA [$^\circ$]	-	5.21

record by the Keysight channel sounder, and the calibration data is obtained in the back-to-back measurements. The system response can be therefore calibrated from the measured CIR data [36]. Based on the CIR data, the PDP can be directly derived by formula (36) in [21], and PL can be calculated by formula (6) in [39]. Space alternating generalized expectation-maximization (SAGE) algorithm [40] is applied to extract MPCs distribution. We also apply the multipath component distance (MCD) algorithm [41] to cluster the extracted MPCs. Then LSCPs including DS, AS (including AASA and EASA) and K-factor are calculated through statistical analysis of SSCPs by formula (9)-(14) in [39]. In order to describe the channel characteristics of substation scenario in a concise manner, PL can be modeled as distance-related variables by close-in (CI) model [42] and SF can be described as a zero mean normal distribution. DS and AS can be modeled as lognormal distributions. Number of clusters can be represented as an ordinary normal distribution. Table II summarizes the simplified channel parameters of the high-voltage substation.

IV. RESULTS AND ANALYSIS

In this section, we present the performance of our proposed channel modeling approach. First, 5 ONNs are generated based on the actual measured channel parameters in the high-voltage substation, and a simulation scenario for algorithm evaluation is described according to the measurement scenario. Second, the LSCPs according to the simulation scenario can be predicted by the generated ONNs. The measured, non-optimized RBF NN predicted and QuaDRiGa simulated LSCPs are compared with the ONN predicted ones to validate the prediction accuracy. Third, the simulated MPCs and corresponding parameters can be obtained based on the simulation scenario as well as the predicted LSCPs, and they are compared with the measured ones. Finally, the CIR matrix can be derived by delays and angles of the simulated MPCs, then the dynamic

PDPs are calculated and compared with the measured and QuaDRiGa simulated ones.

A. ONNs Generation and Simulation Scenario Design

There are totally 27 groups of measured coordinates and corresponding LSCPs in the high-voltage scenario, and we increase the number of datasets by doing interpolation between every two adjacent measured positions, thus 53 groups of datasets can be applied in the ONN generation. According to the generation process in Section II.A 3), the measured data are divided into three parts, 33 groups for training, 8 groups for validation and 12 groups for testing datasets, respectively. The testing datasets are determined first and consisted of three randomly selected segments, each segment contains four consecutive positions. Then 8 validation datasets are randomly selected from the remaining 41 groups of datasets. The reason for choosing the testing datasets in this way is to verify the ability of ONN to predict parameters at consecutive unknown positions. There are five RBF NNs trained by the training datasets, and the optimal values of ξ which minimizes the prediction RMSE of the validation datasets are searched by the SA algorithm. Finally, 5 ONNs are trained by the training and validation datasets as well as the optimal values of ξ .

After generating the ONNs, the simulation scenario can be customized according to the simulation requirements. In this work, the coordinates of TX and RX in the simulation scenario are set consistently with the high-voltage substation for convenient comparison. The simulation scenario including one TX, one moving RX and several determined scatterers. The coordinates of TX are fixed at (0, 0, 2.5). The RX trajectory is set consistently with actual measurement and the total length is set as 150 m. The velocity vector $v_R(t)$ is set as 1 m/s and the data sampling rate is 1 per second, so the distance between two adjacent simulation positions is 1 m. Note that the actual environment in Fig. 7 is too complicated to be accurate modeled, thus in this work, four determined scatterers are set. The first determined scatterer represents the TX equipment, and the approximate coordinates are set near the TX. The second determined scatterer represents ground, and the coordinates are changing with the moving of RX. The specific coordinates are calculated by the geometric relationship. The other two determined scatterers represent the electric power facilities on the both sides of RX trajectory. Note that the electric power facilities are abstracted to two points and the coordinates are estimated by the actual environment in Fig. 7.

B. Performance Analysis of the Predicted LSCPs

The generated ONNs can be applied to predict LSCPs at positions where measured data that are not available. Figs. 9 (a)-(e) show the results of PL, DS, AASA, EASA and number of clusters from measurement, ONN-based simulation, QuaDRiGa simulation, non-optimized RBF NN simulation and spline interpolation, respectively. The positions in training and validation datasets are marked with black square in Fig. 9, while the positions in testing datasets are marked with red square. 150 groups of simulated channels and corresponding

TABLE III

		ERROR ANALYSIS OF LSCP PREDICTION			
	Parameters	ONN-based Model	QuaDRiGa Platform	Non-optimized RBF NN	Spline Interpolation
RMSE	PL [dB]	2.50	4.88	3.63	2.83
	DS [ns]	1.34	4.42	1.65	7.56
	AASA [$^{\circ}$]	0.90	5.28	3.16	1.34
	EASA [$^{\circ}$]	11.95	9.31	8.27	
	Number of Clusters	1.36	4.16	1.25	2.84
MAPE	PL	1.81	4.06	2.43	2.23
	DS	10.98	37.99	11.16	63.98
	AASA	2.38	14.80	8.27	3.42
	[%]	11.46	46.05	37.74	29.40
	Number of Clusters	13.07	53.37	13.65	28.78
		Average	7.94	31.25	14.65
					25.56

LSCPs are generated by QuaDRiGa platform for comparison. Simulated channel generation was reported in our previous work [38]. Non-optimized RBF NNs are trained with default parameter value, i.e., $\xi = 1$. In addition, spline interpolation is performed using the training datasets. We can see from Fig. 9 that the LSCPs predicted by the ONNs are obviously closer to the measured ones than that simulated by other approaches. The QuaDRiGa simulated channels parameters have large errors at certain positions and it cannot be directly used for accurate link-level channel simulation. Besides, the number of clusters is set as a fixed value in the QuaDRiGa platform according to the existing standardization [6]. The LSCPs predicted by non-optimized RBF NN are discontinuous and less accurate compared with these of the ONN-based ones. The LSCPs predicted by spline interpolation are continuous, however the interpolated parameters have large errors as demonstrated in Fig. 9. Furthermore, the interpolation results cannot be used for LSCPs prediction in other scenarios.

In order to quantify the prediction performance of the various approaches of Fig. 9, the prediction errors are calculated and listed in Table III. Since the RMSEs of different LSCPs have different units, we use mean absolute percentage error (MAPE) [31] to evaluate the average prediction error of different approaches. As shown in Table III, the average MAPEs of the ONN-based model, QuaDRiGa platform, non-optimized RBF NN and spline interpolation are 7.94%, 31.25%, 14.65% and 25.56%, respectively, which indicates that the prediction performance of ONN-based model is far better than that of other approaches.

C. Performance Analysis of the Simulated SSCPs

The LSCPs predicted by the ONNs are utilized in the time evolution simulations, and the SSCPs of each MPC are generated by sub-section II. D. Figs. 10 (a) and (b) show the AAoAs distribution from measurement and ONN-based simulation, respectively, while Figs. 11 (a) and (b) show the EAoA distribution. The coordinates of TX, RX and determined scatterers are set as the positions described in subsection A, and only the main rays with strong power are considered in the Fig. 10 and Fig. 11.

We can see from Fig. 10 (b) and Fig. 11 (b) that the AAoA and EAoA distribution of the ONN-based simulated MPCs match very well with the measured ones. In the Fig. 10 (b), the simulated LoS component can be clearly observed around

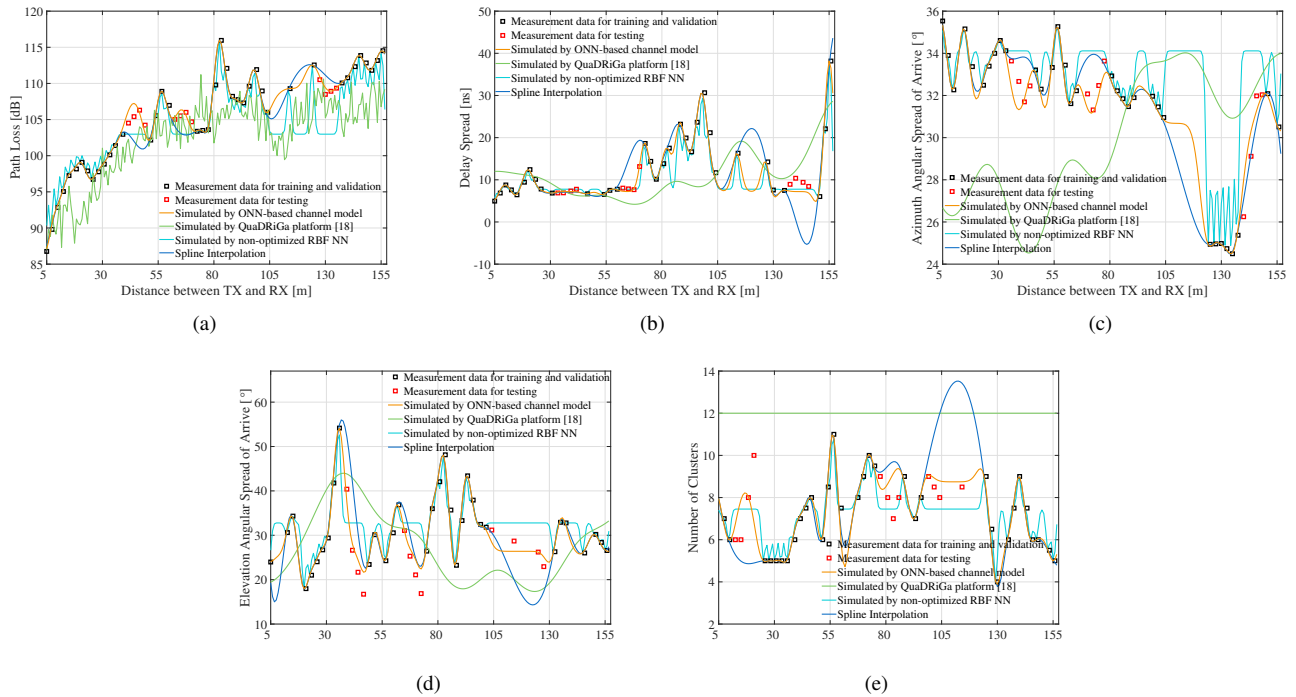


Fig. 9. Comparisons of the LSCPs by measurement, ONN, QuaDRiGa and non-optimized RBF NN based simulations. (a) PL. (b) DS. (c) AASA. (d) EASA. (e) Number of clusters.

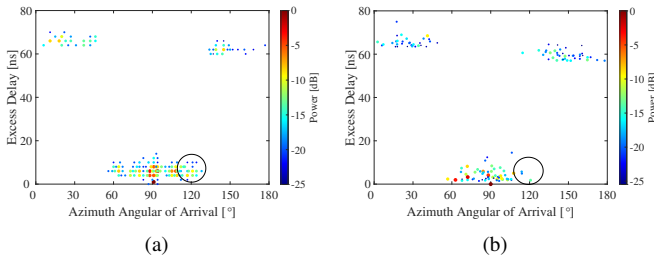


Fig. 10. AAoA distributions. (a) Measurement. (b) ONN-based simulation.

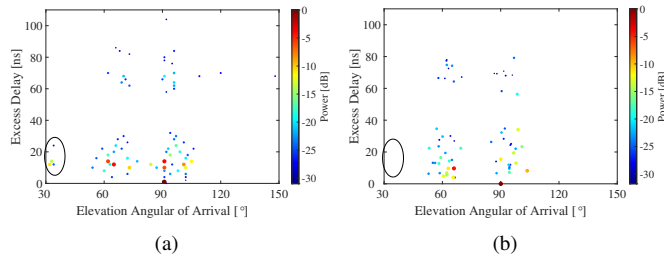


Fig. 11. EAoA distributions. (a) Measurement. (b) ONN-based simulation.

90 degrees in AAoA, and a dominant cluster can be observed next to the LoS component, which is generated by ground and TX equipment. The other two determined clusters can be observed on the both sides of the LoS component with the excess delay about 60 ns, which are generated by the scatterers on the both sides of RX trajectory. Similarly, in Fig. 11 (b), the LoS component can be observed around 90 degrees in EAoA, and one determined cluster can also be observed next to the LoS component which is generated by TX equipment. Besides, the MPC cluster generated by ground appears around

60 degrees in EAoA and 10 ns of excess delay, and the other two determined clusters appears near 60 ns of excess delay. All these observations can verify the correctness and effectiveness of the proposed ONN-based semi-deterministic dynamic model in terms of the distribution of MPCs. However, there are still some discrepancies in the AAoA and EAoA distribution between the measured and simulated MPCs and marked by the black circle in the Fig. 10 and Fig. 11, which are caused by simplification of the environment in the database modeling.

D. Performance Analysis of the Generated CIRs

Finally, the dynamic CIR of each simulation position can be generated through the simulated SSCP in Section II. E, and the accuracy of the simulated CIRs can be validated by PDPs. The PDP is obtained by averaging the CIR of each antenna and then square it. Figs. 12 (a)-(d) depict the dynamic PDPs derived by the measured, ONN-based simulated without randomly generated clusters, ONN-based simulated and QuaDRiGa simulated channels, where x, y-axes and the colorbar denote the propagation delay, distance between TX/RX and normalized power, respectively. In Fig. 12 (b), the LoS component, determined clusters can be observed and distinguished. The LoS component has the smallest delay and the strongest power, and the signal surround LoS component is the combination of rays in determined clusters. However the simulated channels with only determined clusters cannot match the rich multipath in the actual environment. In Fig. 12 (c), randomly generated clusters can be observed with larger delay and weaker power. We can see from Figs. 12 (a) and (c) that the PDPs derived by the ONN-based simulated channels

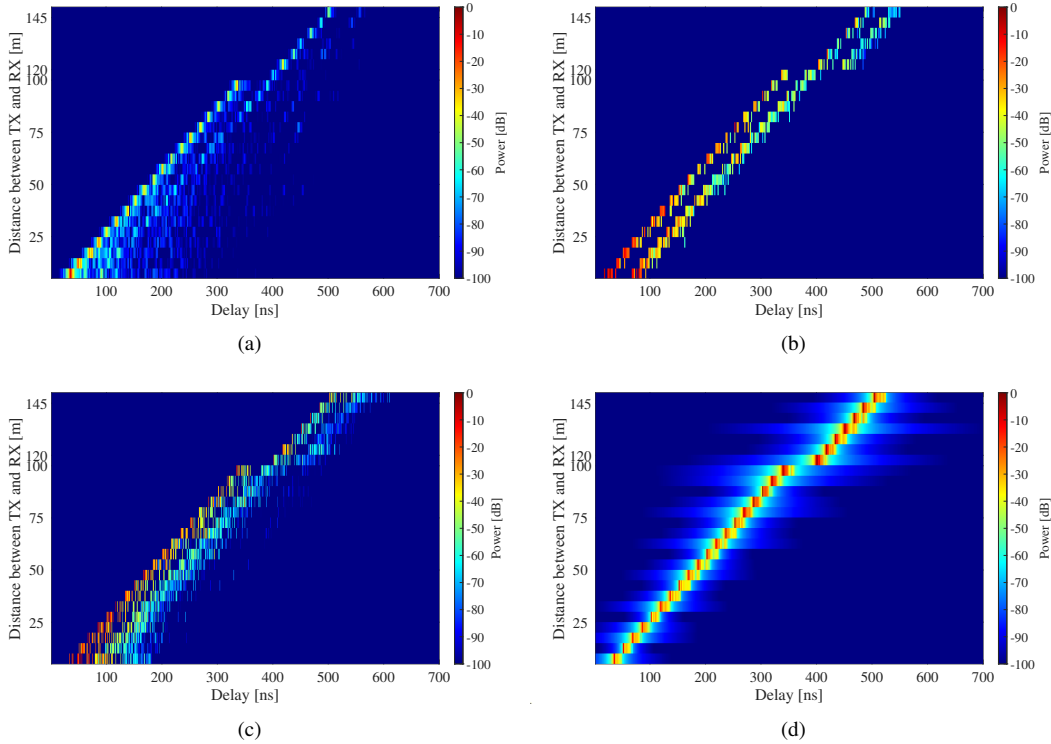


Fig. 12. Dynamic PDPs. (a) Measurement. (b) ONN-based simulation without randomly generated clusters. (c) ONN-based simulation. (d) QuaDRiGa simulation.

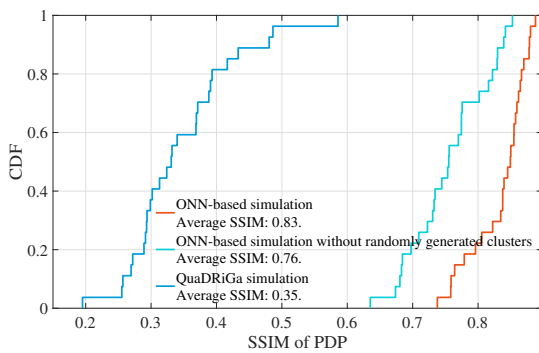


Fig. 13. SSIMs of the dynamic PDPs simulated by different approaches.

agree very well with the measured ones. However, there are still some discrepancies between the ONN-based simulated and measured channels in case of weak randomly generated rays, which is due to the database simplification. We also observe from Figs. 12 (a) and (d) that there is a big difference between the QuaDRiGa simulated and the measured PDPs, as expected.

Furthermore, structural similarity index measure (SSIM) is applied to quantify the accuracy of the ONN-based simulated channels. SSIM is widely applied in image compression and restoration as a measure of figure similarity [43]. The range of SSIM is from 0 to 1, with larger values indicating greater similarity between the two figures. Fig. 13 compares the CDF curves of dynamic PDP SSIM of different simulation approaches. The mean SSIM values of the ONN-based simulation, ONN-based simulation without randomly generated

clusters and QuaDRiGa simulation are 0.83, 0.76 and 0.35, respectively. The results show that the ONN-based simulation with both determined and randomly generated clusters has the highest SSIM, validating the importance of randomly generated clusters. In conclusion, the proposed channel model has the capability to simulate dynamic channels with different kinds of rays, and the simulated PDPs match the measured PDPs very well.

V. CONCLUSION

In this work, a novel semi-deterministic mmWave dynamic channel modeling approach based on the ONN principle is proposed for accurate channel simulation and subsequent network design of the industrial IoTs. The proposed model is able to simulate dynamic mmWave channel with arbitrary customized trajectory of terminal and scatterers. In the channel model, the ONNs are trained by measured large-scale channel parameters and optimized by the SA algorithm to achieve the minimum prediction error. The large-scale channel parameters predicted by the ONNs are applied in the dynamic simulation and channel impulse response matrix are derived according to the geometric relationship, thus all the simulated channel parameters can be consistent with the expected parameters.

To validate the performance of the proposed model, mmWave channel measurements were carried out at a high-voltage substation. Based on the measured channel parameters, five ONNs are generated to predict LSCPs at unknown positions, and the predicted LSCPs are applied in dynamic channel simulation. The performance of the simulation is validated by LSCPs, distribution of MPCs as well as PDPs. The results

show that the average MAPE of the LSCPs simulated by the ONN-based, QuaDRiGa, non-optimized RBF NN and spline interpolation approaches are 7.94%, 31.25%, 14.65% and 25.56%, respectively, which indicates that the prediction performance of ONN-based model is far better than that of other approaches. Both the AAoA and EAoA distribution of the ONN-based simulated MPCs match very well with the measured ones, even though the simulated scenario is very simple. The simulated PDPs are almost consistent with the measured PDPs, which is unachievable for others channel model. Besides, the SSIM values of the ONN-based simulation, ONN-based simulation without randomly generated clusters and QuaDRiGa simulation are 0.83, 0.76 and 0.35, respectively, which indicates that the random component of the ONN-based model is indispensable.

In conclusion, the proposed channel model has the advantage of customization and high accuracy, it can simulate the paths of main MPCs while maintaining the statistical characteristics of the channel, which provides an accurate channel simulation approach for both link-level and system-level in the design and optimization of industrial IoTs.

APPENDIX A DERIVATION OF THE EQUATION 3

RBF NN is a kind of static forward network, which consists of two layers as shown in Fig. 3, namely nonlinear transformation layer and linear combination layer, respectively. The output of the first layer can be expressed as

$$out_{hidden,i} = g(\|\mathbf{q} - w_i\|), \quad (26)$$

where \mathbf{q} is the input vector. w_i is the weight matrix of the nonlinear transformation layer, which is equal to the training input vector matrix. $\|\cdot\|$ denotes 2-norm and $g(\cdot)$ is the nonlinear function and always taken as the Gauss function in RBF NN, which is calculated as

$$g(x) = \exp\left\{-\frac{x^2}{2\xi^2}\right\}, \quad (27)$$

where ξ is the variance of the radial basis function, i.e., the width of the nonlinear transformation function. The value of ξ is adjustable and directly influences the accuracy of prediction, and it is feasible to improve prediction accuracy by finding the optimal value of ξ .

The second layer of RBF NN is the linear combination layer, which is responsible for linearly combining the output of the nonlinear transformation layer. There are two ways to determine the number of hidden nodes. One is based on the training error during the training process, and a hidden node is added if the error is greater than the threshold. The other is to customize directly. By substituting (27) into (26), the output of the linear combination layer can be derived as (28), and the expression of mapping between input and output can be simplified to M

$$\begin{aligned} Y_{k,out} &= M(\mathbf{q}, \xi) = \sum_{i=1}^W (w_{ik} \cdot out_{hidden,i} + b_{ik}) \\ &= \sum_{i=1}^W \left[w_{ik} \cdot \exp\left\{-\frac{(\mathbf{q} - w_i)^T(\mathbf{q} - w_i)}{2\xi^2}\right\} + b_{ik} \right], \quad (28) \end{aligned}$$

where w_{ik} and b_{ik} are adjusted by the gradient descent algorithm. By substituting (28) into (2), the final solution can be translated into (3).

REFERENCES

- [1] X. Zhao *et al.*, "Hybrid Precoding for an Adaptive Interference Decoding SWIPT System With Full-Duplex IoT Devices," *IEEE Internet Things J.*, vol. 7, no. 2, pp. 1164-1177, Feb. 2020.
- [2] R. He *et al.*, "Propagation Channels of 5G Millimeter-Wave Vehicle-to-Vehicle Communications: Recent Advances and Future Challenges," *IEEE Veh. Technol. Mag.*, vol. 15, no. 1, pp. 16-26, Mar. 2020.
- [3] W. Fan *et al.*, "Measured wideband characteristics of indoor channels at centimetric and millimetric bands" *EURASIP Journal on Wireless Communications and Networking*, vol. 1, no. 1, pp. 1-13, Feb. 2016.
- [4] R. He *et al.*, "Wireless Channel Sparsity: Measurement, Analysis, and Exploitation in Estimation," *IEEE Wirel. Commun.*, in press, doi: 10.1109/MWC.001.2000378.
- [5] F. Zhang *et al.*, "Frequency-Invariant Uniform Circular Array for Wideband mm-Wave Channel Characterization," *IEEE Antennas Wireless Propag. Lett.*, vol. 16, pp. 641-644, 2017.
- [6] Study on channel model for frequencies from 0.5 to 100 GHz, 3GPP TR 38.901, V15.0.0, Jun, 2018.
- [7] ITU-R, "Report ITU-R M.2135 Guidelines for Evaluation of Radio Interface Technologies for IMT-Advanced," ITU-R, Tech. Rep., 2009.
- [8] Final Report on Link Level and System Level Channel Models, WINNER II IST-2003-507581, D5.4 ver 1.4, May. 2014.
- [9] 3GPP TR RAN, "Spatial channel model for Multiple Input Multiple Output (MIMO) simulations," 3GPP, Tech. Rep. TR 25.996, Dec. 2015.
- [10] C. F. Yang, B-C. Wu and C-J. Ko, "A ray-tracing method for modeling indoor wave propagation and penetration," *IEEE Trans. on Antennas and Propag.*, vol. 46, no. 6, pp. 907-919, Jun. 1998.
- [11] P. Kyösti *et al.*, "Map-Based Channel Model for Evaluation of 5G Wireless Communication Systems," *IEEE Trans. on Antennas and Propag.*, vol. 65, no. 12, pp. 6491-6504, Dec. 2017.
- [12] IEEE Standard for High Data Rate Wireless Multi-media Networks, IEEE Standard 802.15.3, 2016.
- [13] I. Carton *et al.*, "Validation of 5G METIS map-based channel model at mmwave bands in indoor scenarios," in *Proc. EuCAP*, Apr. 2016, pp. 1-5.
- [14] W. Fan *et al.*, "On Angular Sampling Methods for 3-D Spatial Channel Models," *IEEE Antennas Wireless Propag. Lett.*, vol. 14, pp. 531-534, 2015.
- [15] L. Tian, V. Degli-Esposti, E. M. Vitucci and X. Yin, "Semi-Deterministic Radio Channel Modeling Based on Graph Theory and Ray-Tracing," *IEEE Trans. on Antennas and Propag.*, vol. 64, no. 6, pp. 2475-2486, Jun. 2016.
- [16] S. Jaeckel *et al.*, "QuaDRiGa: A 3-D Multi-Cell Channel Model With Time Evolution for Enabling Virtual Field Trials," *IEEE Trans. on Antennas and Propag.*, vol. 62, no. 6, pp. 3242-3256, Jun. 2014.
- [17] F. Burkhardt *et al.*, "QuaDRiGa: A MIMO channel model for land mobile satellite," in *Proc. EuCAP*, Apr. 2014, pp. 1274-1278.
- [18] Fraunhofer Heinrich Hertz Institute, "The Implementation of Quasi Deterministic Radio Channel Generator (QuaDRiGa), v2.4.0," 2020.
- [19] S. Wu *et al.*, "A General 3-D Non-Stationary 5G Wireless Channel Model," *IEEE Trans. Commun.*, vol. 66, no. 7, pp. 3065-3078, Jul. 2018.
- [20] R. He *et al.*, "Geometrical-Based Modeling for Millimeter-Wave MIMO Mobile-to-Mobile Channels," *IEEE Trans. Veh. Technol.*, vol. 67, no. 4, pp. 2848-2863, Apr. 2018.
- [21] H. Chang *et al.*, "A Novel Non-Stationary 6G UAV-to-Ground Wireless Channel Model with 3D Arbitrary Trajectory Changes," *IEEE Internet Things J.*, in press, doi: 10.1109/JIOT.2020.3018479.
- [22] G. P. Ferreira, L. J. Matos and J. M. M. Silva, "Improvement of Outdoor Signal Strength Prediction in UHF Band by Artificial Neural Network," *IEEE Trans. on Antennas and Propag.*, vol. 64, no. 12, pp. 5404-5410, Dec. 2016.
- [23] M. Ayadi, A. Ben Zineb and S. Tabbane, "A UHF Path Loss Model Using Learning Machine for Heterogeneous Networks," *IEEE Trans. on Antennas and Propag.*, vol. 65, no. 7, pp. 3675-3683, Jul. 2017.
- [24] N. Faruk *et al.*, "Path Loss Predictions in the VHF and UHF Bands Within Urban Environments: Experimental Investigation of Empirical, Heuristics and Geospatial Models," *IEEE Access*, vol. 7, pp. 77293-77307, 2019.
- [25] X. Zhao *et al.*, "Neural network and GBSM based time-varying and stochastic channel modeling for 5G millimeter wave communications," *China Communications*, vol. 16, no. 6, pp. 80-90, June 2019.

- [26] J. Lee, M. Y. Kang and S. Kim, "Path Loss Exponent Prediction for Outdoor Millimeter Wave Channels through Deep Learning," in *Proc. IEEE WCNC.*, Apr. 2019, pp. 1-5.
- [27] Y. Yang *et al.*, "Generative-Adversarial-Network-Based Wireless Channel Modeling: Challenges and Opportunities," *IEEE Commun. Mag.*, vol. 57, no. 3, pp. 22-27, Mar. 2019.
- [28] L. Bai *et al.*, "Predicting wireless mmWave massive MIMO channel characteristics using machine learning algorithms," *Wireless Communications and Mobile Computing*, vol. 2018, Aug. 2018.
- [29] J. Huang *et al.*, "A Big Data Enabled Channel Model for 5G Wireless Communication Systems," *IEEE Trans. Big Data*, vol. 6, no. 2, pp. 211-222, Jun. 2020.
- [30] L. Azpilicueta *et al.*, "A Ray Launching-Neural Network Approach for Radio Wave Propagation Analysis in Complex Indoor Environments," *IEEE Trans. on Antennas and Propag.*, vol. 62, no. 5, pp. 2777-2786, May. 2014.
- [31] X. Zhao *et al.*, "Playback of 5G and Beyond Measured MIMO Channels by an ANN-Based Modeling and Simulation Framework," *IEEE J. Sel. Areas Commun.*, vol. 38, no. 9, pp. 1945-1954, Sep. 2020.
- [32] P. Zhang *et al.*, "RBF-MLMR: A Multi-Label Metamorphic Relation Prediction Approach Using RBF Neural Network," *IEEE Access*, vol. 5, pp. 21791-21805, 2017.
- [33] S. Kirkpatrick, C. Gelatt, and M. Vechhi, "Optimization by simulated annealing," *Science*, [35] vol. 220, no. 4598, pp. 671–680, May. 1983.
- [34] H. Han *et al.*, "An Adaptive-PSO-Based Self-Organizing RBF Neural Network," *IEEE Trans. Neural Netw. Learning Sys.*, vol. 29, no. 1, pp. 104-117, Jan. 2018.
- [35] X. Cai *et al.*, "An Empirical Air-to-Ground Channel Model Based on Passive Measurements in LTE," *IEEE Trans. Veh. Technol.*, vol. 68, no. 2, pp. 1140-1154, Feb. 2019.
- [36] Zhu Wen *et al.*, "mmWave channel sounder based on COTS instruments for 5G and indoor channel measurement," in *Proc. IEEE WCNC.*, Apr. 2016, pp. 37-43.
- [37] F. Zhang *et al.*, "Virtual Large-Scale Array Beamforming Analysis Using Measured Subarray Antenna Patterns," *IEEE Access*, vol. 5, pp. 19812-19823, 2017.
- [38] Z. Fu *et al.*, "5G Millimeter Wave Channel Modeling and Simulations for a High-Voltage Substation," in *Proc. IEEE ISPEC.*, Nov. 2019, pp. 1822-1826.
- [39] X. Zhao *et al.*, "Channel Measurements, Modeling, Simulation and Validation at 32 GHz in Outdoor Microcells for 5G Radio Systems," *IEEE Access*, vol. 5, pp. 1062-1072, 2017.
- [40] B. H. Fleury *et al.*, "Channel parameter estimation in mobile radio environments using the SAGE algorithm," *IEEE J. Sel. Areas Commun.*, vol. 17, no. 3, pp. 434-450, Mar. 1999.
- [41] X. Yin, C. Ling and M. D. Kim, "Experimental Multipath-Cluster Characteristics of 28-GHz Propagation Channel," *IEEE Access*, [40]vol. 3, pp. 3138-3150, 2015.
- [42] T. S. Rappaport *et al.*, "Wideband Millimeter-Wave Propagation Measurements and Channel Models for Future Wireless Communication System Design," *IEEE Trans. Commun.*, vol. 63, no. 9, pp. 3029-3056, Sep. 2015.
- [43] Z. Wang and Q. Li, "Information Content Weighting for Perceptual Image Quality Assessment," *IEEE Trans. on Image Process.*, vol. 20, no. 5, May 2011, pp. 1185-1198.